Ab initio analysis of plasmon dispersion in sodium under pressure

Julen Ibañez-Azpiroz,[1,2] Bruno Rousseau,[3] Asier Eiguren,[1,2] and Aitor Bergara[1,2,4]

[1]*Materia Kondentsatuaren Fisika Saila, Zientzia eta Teknologia Fakultatea, Euskal Herriko Unibertsitatea, 644 Postakutxatila, 48080 Bilbao, Basque Country, Spain*

[2]*Donostia International Physics Center (DIPC), Paseo Manuel de Lardizabal 4, 20018 Donostia/San Sebastian, Spain*

[3]*Département de physique et Regroupement québécois sur les matériaux de pointe (RQMP), Université de Montréal, C. P. 6128 Succursale Centre-ville, Montréal (Québec), Canada H3C 3J7*

[4]*Centro de Física de Materiales CFM - Materials Physics Center MPC, Centro Mixto CSIC-UPV/EHU, Edificio Korta, Avenida de Tolosa 72, 20018 Donostia, Basque Country, Spain*

(Received 6 November 2013; revised manuscript received 9 January 2014; published 5 February 2014)

We present an *ab initio* study of the electronic response function of sodium in its five known metallic phases from 0 to 180 GPa at room temperature. The considered formalism is based on a interpolation scheme within time-dependent density functional theory that uses maximally localized Wannier functions, providing an accurate sampling of the reciprocal space. Besides showing an excellent agreement with inelastic x-ray scattering experiments [Phys. Rev. Lett. **107**, 086402 (2011), Proc. Natl. Acad. Sci. USA **108**, 20434 (2011)], our calculations reveal that the drastic decrease of the optical reflectivity measured in the high pressure phases oP8 and tI19 [Proc. Natl. Acad. Sci. USA **106**, 6525 (2009)] is associated with a new low-energy plasmon arising from collective interband excitations. Additionally, our calculations predict the existence of an anisotropic interband plasmon in the stability pressure range of fcc Na (65 to 105 GPa).

DOI: 10.1103/PhysRevB.89.085102 PACS number(s): 31.15.ac, 78.20.Bh, 71.45.Gm

I. INTRODUCTION

Sodium is one of the closest realizations of the free-electron gas that can be found in solid-state materials. Under compression, however, the simple metal behavior of Na is deeply modified by non-free-electron-like features of its band structure; these are mainly associated with the increasing electronic hybridization of the chemical bondings and the strong nonlocal character of the pseudopotential, among other causes [1]. As a consequence, sodium under pressure develops a variety of unexpected processes including phase transitions to extremely complex structures [2], loss of the metallic character [3], or anomalies in the optical response to external fields [4,5]. These remarkable phenomena challenge the classical viewpoint that pressure should make simple metals even simpler.

According to room temperature x-ray diffraction experiments [2,3,5,6], sodium undergoes a series of structural phase transformations from 0 to ∼180 GPa before it experiences a metal-insulator transition that suppresses its metallic properties. Over this wide pressure range, sodium first adopts the bcc structure (0 to 65 GPa), followed by the fcc (65 to 105 GPa), the cI16 (105 to 118 GPa), the oP8 (118 to 125 GPa), and the tI19 (125 to ∼180 GPa) configurations [7]. Similar to what happens in other *a priori* simple metals, such as lithium [8] or calcium [9], the metallic properties of sodium at high pressures are strongly modified. In particular, the high and uniform reflectivity (characteristic of good metals) of the bcc, fcc, and cI16 phases has been measured to drop drastically in the high pressure phases oP8 and tI19, accompanied by a decrease of the metallic character [4]. The origin of such behavior may lie on the emergence of low-energy interband plasmons arising from the increasing localization of the valence electrons [10], as it is the case of Li and Ca [11,12].

In this paper we perform a detailed *ab initio* analysis of the electronic properties of Na in a pressure domain ranging from 0 to 180 GPa, covering all the metallic phases of sodium at room temperature. In the spirit of Ref. [13] we employ a formalism based on Wannier interpolation to obtain the electronic linear response within time-dependent density functional theory (TDDFT). This approach allows us to perform a very accurate sampling of the relevant functions in reciprocal space, which is essential for describing the low-energy excitations that determine the response function. As it will be shown, our calculations predict the existence of a very low-energy plasmon in the oP8 and tI19 phases of sodium that explains the anomalous optical properties measured at the corresponding pressures [4]. In addition, our analysis of the lower pressure phase (fcc) indicates that sodium develops an anisotropic interband plasmon originating from a band structure effect along the ΓL direction.

The paper is organized as follows. In Sec. II the Wannier-based interpolation scheme for calculating the plasmon dispersion within TDDFT is presented, along with the details regarding the ground state *ab initio* calculations. The method is applied to calculate the plasmon dispersion in the metallic phases of Na; results and their analysis are presented in Sec. III. A summary and conclusions are presented in Sec. IV. Unless otherwise stated, atomic units are used throughout the work ($\hbar = m_e = e^2 = 4\pi\epsilon_0 = 1$).

II. THEORETICAL FRAMEWORK

In this section we review the formalism for calculating the dispersion of collective charge excitations in solids within TDDFT [14,15]. The key ingredient for such a task is the interacting response function, which describes the variation of the electronic density induced by an external time-dependent potential. The expression for this quantity is

given by

$$\chi_{\mathbf{q}}(\mathbf{r},\mathbf{r}',\omega) = \chi_{\mathbf{q}}^{\mathrm{KS}}(\mathbf{r},\mathbf{r}',\omega) + \frac{1}{\Omega}\int d\mathbf{r}_1 \frac{1}{\Omega}\int d\mathbf{r}_2 \times \chi_{\mathbf{q}}^{\mathrm{KS}}(\mathbf{r},\mathbf{r}_1,\omega)K_{\mathbf{q}}(\mathbf{r}_1,\mathbf{r}_2,\omega)\chi_{\mathbf{q}}(\mathbf{r}_2,\mathbf{r}',\omega), \quad (1)$$

where Ω denotes the unit cell volume. In Eq. (1) $\chi_{\mathbf{q}}^{\mathrm{KS}}(\mathbf{r},\mathbf{r}',\omega)$ represents the noninteracting Kohn-Sham (KS) response function for a given frequency ω and momentum $\mathbf{q}$. The term $K_{\mathbf{q}}(\mathbf{r},\mathbf{r}',\omega)$ is the kernel that takes into account the electron-electron interactions:

$$K_{\mathbf{q}}(\mathbf{r},\mathbf{r}',\omega) = \frac{e^2}{|\mathbf{r}-\mathbf{r}'|} + f_{\mathbf{q}}^{\mathrm{xc}}(\mathbf{r},\mathbf{r}',\omega). \quad (2)$$

The first term in Eq. (2) is the Coulomb interaction associated with the electronic charge, while $f_{\mathbf{q}}^{\mathrm{xc}}(\mathbf{r},\mathbf{r}',\omega)$ contains the exchange and correlation effects. In the present work, $f_{\mathbf{q}}^{\mathrm{xc}}(\mathbf{r},\mathbf{r}',\omega)$ has been approximated within the PZ-LDA parametrization [16,17].

In terms of the single-particle KS orbitals $\psi_{n\mathbf{k}}(\mathbf{r})$, the expression of the noninteracting KS response function is given by [18]

$$\chi_{\mathbf{q}}^{\mathrm{KS}}(\mathbf{r},\mathbf{r}',\omega) = \sum_{n_1,n_2}\sum_{\mathbf{k}}^{1\mathrm{BZ}} \frac{f(\xi_{n_1\mathbf{k}}) - f(\xi_{n_2\mathbf{k}+\mathbf{q}})}{\omega + \xi_{n_1\mathbf{k}} - \xi_{n_2\mathbf{k}+\mathbf{q}} + i\delta} \times \psi_{n_1\mathbf{k}}^*(\mathbf{r})\psi_{n_2\mathbf{k}+\mathbf{q}}(\mathbf{r})\psi_{n_2\mathbf{k}+\mathbf{q}}^*(\mathbf{r}')\psi_{n_1\mathbf{k}}(\mathbf{r}'), \quad (3)$$

where δ is an infinitesimal positive parameter ensuring causality. In Eq. (3) $\mathbf{k}$ is constrained to the first Brillouin zone (1BZ), n_1 and n_2 are band indices, $\xi_{n\mathbf{k}} = \epsilon_{n\mathbf{k}} - \mu$ with $\epsilon_{n\mathbf{k}}$ a KS eigenvalue and μ the chemical potential, and $f(\xi)$ represents the Fermi-Dirac distribution function.

A. Maximally localized Wannier functions

An appropriate basis set for calculating $\chi_{\mathbf{q}}^{\mathrm{KS}}(\mathbf{r},\mathbf{r}',\omega)$ can be constructed in terms of maximally localized Wannier functions (MLWFs) [13]. The relationship between the Wannier states and the KS states is given by

$$W_n(\mathbf{r}-\mathbf{R}) = \frac{1}{\sqrt{N}}\sum_{m\mathbf{k}} e^{-i\mathbf{k}\cdot\mathbf{R}}\psi_{m\mathbf{k}}(\mathbf{r})\mathbf{U}_{mn}(\mathbf{k}). \quad (4)$$

In Eq. (4) $\mathbf{R}$ denotes a periodic lattice vector, while $\mathbf{U}(\mathbf{k})$ is a unitary matrix in band indices [19]. In practical calculations, the sum in Eq. (4) is over a $\mathbf{k}$-point mesh that must accurately reproduce the electronic band structure of the system. The first-principles calculation of the ground-state orbitals in that mesh usually requires a substantial computational effort. However, once the Wannier functions have been constructed via Eq. (4), quantities such as eigenvalues, eigenfunctions, or the above mentioned unitary matrices can be interpolated into a much finer $\mathbf{k}$-point mesh using a computationally inexpensive fast Fourier transform algorithm.

The noninteracting response function defined in Eq. (3) can be cast into the following form with the aid of the Wannier functions:

$$\chi_{\mathbf{q}}^{\mathrm{KS}}(\mathbf{r},\mathbf{r}',\omega) = \sum_{IJ}[B_{I,\mathbf{q}}(\mathbf{r})]\boldsymbol{\chi}_{IJ}^{\mathrm{KS}}(\mathbf{q},\omega)[B_{J,\mathbf{q}}(\mathbf{r})]^*, \quad I \equiv \{m_1,m_2,\mathbf{R}\}, \quad J \equiv \{m_3,m_4,\mathbf{R}'\}, \quad (5)$$

where the lattice periodic functions $\{B_{I,\mathbf{q}}(\mathbf{r})\}$, which we will henceforth refer to as the bare basis, are given by

$$B_{I,\mathbf{q}}(\mathbf{r}) = \frac{\Omega}{N}\sum_{\mathbf{R}'} e^{i\mathbf{q}\cdot(\mathbf{R}'-\mathbf{r})}W_{m_1}^*(\mathbf{r}-[\mathbf{R}'-\mathbf{R}])W_{m_2}(\mathbf{r}-\mathbf{R}'). \quad (6)$$

We notice that the bare basis of Eq. (6) has a trivial dependence on the external momentum $\mathbf{q}$, as it only enters in the exponential factor. Thus, once the product $W_{m_1}^*(\mathbf{r}-[\mathbf{R}'-\mathbf{R}])W_{m_2}(\mathbf{r}-\mathbf{R}')$ is calculated and stored, the bare basis for different momenta is straightforwardly obtained. This allows us to efficiently map the evolution of the response function as a function of $\mathbf{q}$, which is of critical importance when analyzing the dispersion of plasmons.

The coefficients $\boldsymbol{\chi}_{IJ}^{\mathrm{KS}}(\mathbf{q},\omega)$ entering Eq. (5) do not explicitly depend on the Wannier functions, but only on the unitary matrices,

$$\boldsymbol{\chi}_{IJ}^{\mathrm{KS}}(\mathbf{q},\omega) = \frac{1}{\Omega}\sum_{\mathbf{k}}^{1\mathrm{BZ}} e^{i\mathbf{k}\cdot(\mathbf{R}-\mathbf{R}')} \times \sum_{n_1,n_2}\frac{f(\xi_{n_1\mathbf{k}}) - f(\xi_{n_2\mathbf{k}+\mathbf{q}})}{\hbar\omega + \xi_{n_1\mathbf{k}} - \xi_{n_2\mathbf{k}+\mathbf{q}} + i\delta} \times \mathbf{U}_{n_1m_1}(\mathbf{k})\mathbf{U}_{m_2n_2}^{\dagger}(\mathbf{k}+\mathbf{q})\mathbf{U}_{m_3n_1}^{\dagger}(\mathbf{k})\mathbf{U}_{n_2m_4}(\mathbf{k}+\mathbf{q}). \quad (7)$$

In practice we have collected all the $\mathbf{k}$-dependent quantities into the above coefficients, given that the bare basis functions are $\mathbf{k}$ independent. It is noteworthy that all the ingredients in Eq. (7) can be calculated on a fine $\mathbf{k}$ mesh using the Wannier interpolation scheme, allowing a very fine sampling of $\boldsymbol{\chi}_{IJ}^{\mathrm{KS}}(\mathbf{q},\omega)$.

We notice that in contrast to the bare basis, the dependence of $\boldsymbol{\chi}_{IJ}^{\mathrm{KS}}(\mathbf{q},\omega)$ on the external momentum is not trivial as it involves terms like $\mathbf{U}_{mn}(\mathbf{k}+\mathbf{q})$, $\epsilon_{n\mathbf{k}+\mathbf{q}}$, and $f_{n\mathbf{k}+\mathbf{q}}$. In principle, these terms should be calculated *ab initio* for each different $\mathbf{q}$. However, if the point $\mathbf{k}+\mathbf{q}$ lies inside the interpolated grid, then the $\mathbf{q}$-dependent quantities of Eq. (7) are directly available. In practice, Wannier interpolation allows to consider such fine $\mathbf{k}$ meshes so that choosing $\mathbf{q}$ inside the interpolated grid does not represent a limitation.

From the computational point of view, it is of practical interest to express the central equation describing the interacting response function [Eq. (1)] as a matrix equation. Let us consider the kets $|B_{I,\mathbf{q}}\rangle$ associated with the bare basis functions and represent the KS response function as

$$\hat{\boldsymbol{\chi}}_{\mathbf{q}}^{\mathrm{KS}} = \sum_{IJ}|B_{I,\mathbf{q}}\rangle\,\boldsymbol{\chi}_{IJ}^{\mathrm{KS}}(\mathbf{q},\omega)\,\langle B_{J,\mathbf{q}}|\,. \quad (8)$$

In this way Eq. (1) can be written as a matrix equation,

$$\hat{\boldsymbol{\chi}}_{\mathbf{q}} = \left(\hat{\mathbf{1}} - \hat{\boldsymbol{\chi}}_{\mathbf{q}}^{\mathrm{KS}}\cdot\hat{\boldsymbol{K}}_{\mathbf{q}}\right)^{-1}\cdot\hat{\boldsymbol{\chi}}_{\mathbf{q}}^{\mathrm{KS}}. \quad (9)$$

The above matrix equation must be truncated into a finite size problem in order to be solved numerically. Given that the basis functions $B_{I,\mathbf{q}}(\mathbf{r})$ are not linearly independent, it is ineffective to compute all the coefficients $\boldsymbol{\chi}_{IJ}^{\mathrm{KS}}(\mathbf{q},\omega)$ independently. Instead, it is convenient to establish a minimal basis set that describes the essential physics of the problem.

Plasmons are described as peaks in $\mathrm{Im}\,\hat{\boldsymbol{\chi}}_{\mathbf{q}}(\omega)_{\mathbf{00}}$ [20,21]. Therefore, it is sensible to include the function $|1\rangle$ (i.e., a plane wave with $\mathbf{G} = \mathbf{0}$) in the minimal basis set. In addition, crystal local field effects (CLFE) often play an important role in determining the plasmon dispersion; usually, wave vectors other than $\mathbf{q}$ are needed for describing the spatial variation of external fields inside the solid due to the inhomogeneity of the system [18,22]. Generally the use of a finite number of $\mathbf{G}$ vectors properly describes the CLFE. Therefore, we include plane waves

$$\frac{1}{\sqrt{\Omega}} e^{i\mathbf{G}\cdot\mathbf{r}} \rightarrow |\mathbf{G}\rangle \tag{10}$$

in the minimal basis set; the number of $\mathbf{G}$ vectors to include is a parameter to be converged. Thus, the minimal basis should span the same functional space as the set of functions:

$$|g_i\rangle \in \{|1\rangle, \{|\mathbf{G}\rangle\}\}. \tag{11}$$

We define the minimal basis functions as

$$|b_i\rangle = \sum_j |g_j\rangle\, g_{ij}, \quad \langle g_j|b_i\rangle = g_{ij}, \quad \langle b_i|b_j\rangle = \delta_{ij}. \tag{12}$$

In this way, the self-consistent Eq. (9) regarding the interacting response function can be solved by projecting the relevant functions into the minimal basis set,

$$[\hat{\boldsymbol{\chi}}_{\mathbf{q}}]_{ij} \simeq \sum_l \left[\left(\hat{\mathbf{1}} - \hat{\boldsymbol{\chi}}^{\mathrm{KS}}_{\mathbf{q}} \cdot \hat{\boldsymbol{K}}_{\mathbf{q}}\right)^{-1}\right]_{il} \left[\hat{\boldsymbol{\chi}}^{\mathrm{KS}}_{\mathbf{q}}\right]_{lj}, \tag{13}$$

where the latin indices refer to the functions $b_i(\mathbf{r})$. Finally, for future analysis of plasmon-related properties, it is convenient to write down the expression of the inverse dielectric matrix in this subspace,

$$\left[\hat{\boldsymbol{\epsilon}}^{-1}_{\mathbf{q}}\right]_{ij} \simeq \delta_{ij} + \sum_l [\hat{\boldsymbol{K}}_{\mathbf{q}}]_{il} \cdot [\hat{\boldsymbol{\chi}}_{\mathbf{q}}]_{lj}. \tag{14}$$

B. Computational details

The DFT calculations for the ground state eigenvalues and eigenfunctions have been performed using the QUANTUM-ESPRESSO package [23], with plane waves as the basis set for the expansion of the KS orbitals. The cutoff energy used to determine the size of the plane wave basis has been 120 Ry. The exchange-correlation energy has been approximated within the LDA parametrization [16,17] and the 1BZ has been sampled on a $12 \times 12 \times 12$ $\mathbf{k}$-point mesh [24].

The electron-ion interaction has been modeled considering a nonrelativistic pseudopotential for Na generated with the OPIUM code [25] and tested with all-electron calculations performed with the ELK code [26]. We have included $2s^2 2p^6 3s^1$ states in the valence in order to properly describe short range effects induced by pressure.

The postprocessing step for obtaining the MLWFs has been done using the WANNIER90 code [27]. We have taken into account all bands up to 35 eV above the Fermi level. Once the MLWFs have been constructed, the necessary ingredients for calculating the interacting response function, namely eigenvalues, occupation factors, and rotation unitary matrices, have been interpolated on a fine $80 \times 80 \times 80$ $\mathbf{k}$-point mesh. Regarding CLFE, the use of three reciprocal lattice shells has yielded converged results in all the phases. In our calculations we find that CLFE have a minor effect on the plasmon energy, which is modified by less than 2% by the inclusion of CLFE in all cases.

The effects of compression have been simulated by reducing the lattice parameter. For the bcc and fcc configurations, we have used the experimental parameters extracted from the equation of state of sodium at the corresponding pressures [28]. For the cI16 and oP8 phases, we have considered the lattice parameters reported in high pressure experiments [2,4]. For the tI19 phase, sodium adopts an incommensurate host-guest configuration with 16 host atoms distributed in a tetragonal bcc structure [2]. We have modeled this incommensurate phase by the closely related commensurate tI20 structure, containing 20 atoms per unit cell [4]. Due to the wide stability pressure range of tI19 (125 to 180 GPa), we have analyzed the evolution of its electronic properties at different pressures. As for this structure there is no accessible experimental lattice parameters at the present time, we have used the theoretically calculated ones: $a = 6.59$, 6.46, and 6.34 a.u. and $c = 3.65$, 3.54, and 3.42 a.u. for 125, 150, and 180 GPa, respectively.

Regarding the calculation of the KS response function, we have explicitly computed the absorptive part:

$$\begin{aligned}\mathrm{Im}\,\chi^{\mathrm{KS}}_{\mathbf{q}}(\mathbf{r},\mathbf{r}',\omega) = \sum_{n_1,n_2} \sum_{\mathbf{k}}^{1\mathrm{BZ}} [f(\xi_{n_1\mathbf{k}}) - f(\xi_{n_2\mathbf{k}+\mathbf{q}})] \\ \times \psi^*_{n_1\mathbf{k}}(\mathbf{r})\psi_{n_2\mathbf{k}+\mathbf{q}}(\mathbf{r})\psi^*_{n_2\mathbf{k}+\mathbf{q}}(\mathbf{r}')\psi_{n_1\mathbf{k}}(\mathbf{r}') \\ \times \delta(\hbar\omega + \xi_{n_1\mathbf{k}} - \xi_{n_2\mathbf{k}+\mathbf{q}}),\end{aligned} \tag{15}$$

while the reactive part $\mathrm{Re}\,\chi^{\mathrm{KS}}_{\mathbf{q}}(\mathbf{r},\mathbf{r}',\omega)$ has been obtained applying the Kramers-Kronig relations [29]. The Dirac δ distribution appearing in Eq. (15) has been approximated by a Gaussian function. At each $\mathbf{k}$ point the width of the Gaussian function has been adapted to the steepness of the integrand of Eq. (15) [13]. The necessary band gradients have been straightforwardly obtained using Wannier interpolation [30].

III. RESULTS AND DISCUSSION

In this section we present the calculated electronic properties of sodium using the formalism introduced in Sec. II. Our calculations cover a pressure range from 0 to 180 GPa. We divide the analysis in two different parts, namely the 0–105 GPa range, analyzed in Sec. III A, and the 105–180 GPa range, analyzed in Sec. III B. In the first one, sodium adopts the bcc and fcc structures, which are considerably simpler than the ones arising above 105 GPa.

A. Simple phases of sodium

1. The bcc phase (0–65 GPa)

We begin analyzing the electron-hole and collective excitations of bcc Na at ambient pressure. In Fig. 1(a) we show the calculated dynamical structure factor,

$$S(\mathbf{q},\omega) = -\frac{|\mathbf{q}|^2}{4\pi^2}\,\mathrm{Im}\,\hat{\boldsymbol{\epsilon}}^{-1}_{\mathbf{q}}(\omega)_{\mathbf{00}}, \tag{16}$$

while the electron-hole excitation spectrum is analyzed in Fig. 1(b), where we show the calculated $\mathrm{Im}\,\hat{\boldsymbol{\chi}}^{\mathrm{KS}}_{\mathbf{q}}(\omega)_{\mathbf{00}}$.

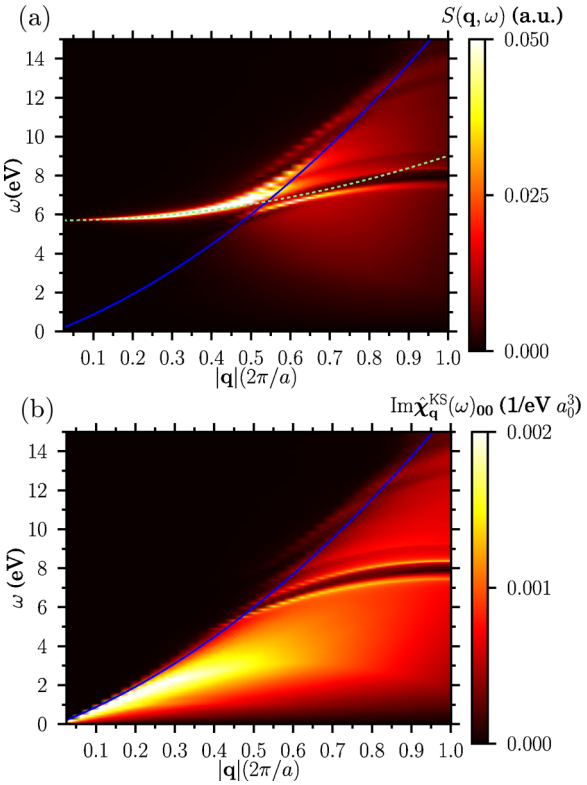

FIG. 1. (Color online) (a) and (b) Dynamical structure factor and imaginary part of the KS response function of bcc Na at ambient pressure along the ΓP direction, respectively. In (a), the dashed (green) line depicts the plasmon dispersion in the RPA free-electron model [Eq. (17)], while the solid (blue) line in (a) and (b) represents the boundary $q^2/2m_{\mathrm{eff}} + q v_F$ of the intraband electron-hole excitations.

Figure 1 shows a quantitative agreement between our calculations and the predictions of the free-electron model. For low values of the momentum, the calculated plasmon dispersion [Fig. 1(a)] follows the classical RPA expression [22]:

$$E_p(q) = \omega_p + \frac{\alpha_{\mathrm{RPA}}}{m_{\mathrm{eff}}} q^2, \tag{17}$$

with m_{eff} as the effective electron mass, $\alpha_{\mathrm{RPA}} = \frac{3}{5}\frac{E_F}{m_{\mathrm{eff}}\omega_p}$ as a dimensionless dispersion constant, E_F as the Fermi energy and $\omega_p = \sqrt{4\pi n/m_{\mathrm{eff}}}$ as the plasmon energy in the free-electron model, where n is the valence electron density. At ambient pressure, the free-electron-like plasmon for $\mathbf{q} \to 0$ is expected to be located around $E_p(q \to 0) = \omega_p \simeq 5.8$ eV, in good agreement with the calculated value ~5.7 eV. For finite values of the momentum, Fig. 1(a) displays a smooth parabolic dispersion of the plasmon until it decays into the electron-hole continuum at around 6.3 eV. This is clear from Fig. 1(b), where the border of the electron-hole continuum can be inferred from the free-electron model prediction,

$$\omega \leqslant \frac{q^2}{2m_{\mathrm{eff}}} + q v_F, \tag{18}$$

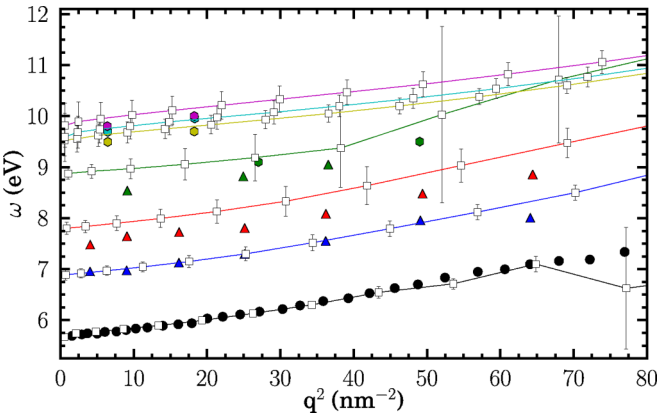

FIG. 2. (Color online) Plasmon dispersion $E_p(q^2)$ of bcc and fcc Na. We include data from the bcc phase for 0 (black), 8 (blue), 16 (red), and 43 (green) GPa, while in the fcc phase we include calculations at 75 (yellow), 87 (cyan), and 97 (purple) GPa. Empty squares represent our *ab initio* results, with the calculated plasmon linewidth indicated by the markers. The full lines are simple guides to the eye. Circles denote experimental EELS data taken from Ref. [31], while triangles and hexagons denote experimental IXS data taken from Refs. [32] and [33], respectively. The experimental energy resolution of the circles, triangles, and hexagons are 0.16, 0.6, and 0.1 eV, respectively.

with $v_F = \sqrt{2E_F/m_{\mathrm{eff}}}$ as the Fermi velocity. The above dispersion is shown as a solid blue line in Fig. 1(b), matching very well the calculated border.

In Fig. 2 we present the calculated plasmon dispersion in the bcc phase at 0, 8, 16, and 43 GPa extracted from the position of the peaks in the energy-loss function at these pressures. We have plotted the plasmon energies as a function of q^2, since we expect the parabolic dependence of Eq. (17). Overall we find that the dispersion is indeed very close to parabolic at all pressures, though the results at 0 and 43 GPa show a slight slope change at $q^2 \sim 40\,\mathrm{nm}^{-2}$ and $q^2 \sim 65\,\mathrm{nm}^{-2}$, respectively. As revealed by the calculated linewidth, which increases up to ~2 eV at the mentioned momenta, the change of slope is due to the damping of the plasmon, which ceases to be a well defined collective excitation at those points.

For comparison, in Fig. 2 we have included experimental data obtained by electron energy-loss spectroscopy (EELS) at ambient pressure [31] and inelastic x-ray scattering (IXS) at higher pressures [32,33]. As it can be appreciated, our results are essentially in agreement with the experimental data. In the case of 0 and 8 GPa, both the calculated energies and dispersion slopes are practically identical to the IXS data of Ref. [32]. At 16 and 43 GPa, the calculated peaks are slightly overestimated by ~0.3 eV with respect to IXS data of Ref. [32], showing a better agreement with the IXS data at 43 GPa of Ref. [33]. The deviation is barely larger than the energy resolution (0.6 eV) of the IXS data of Ref. [32]. Furthermore, the agreement between the calculated and experimental slopes at these two pressures indicates the adequacy of our calculations for describing the collective electronic properties of the system at different pressures.

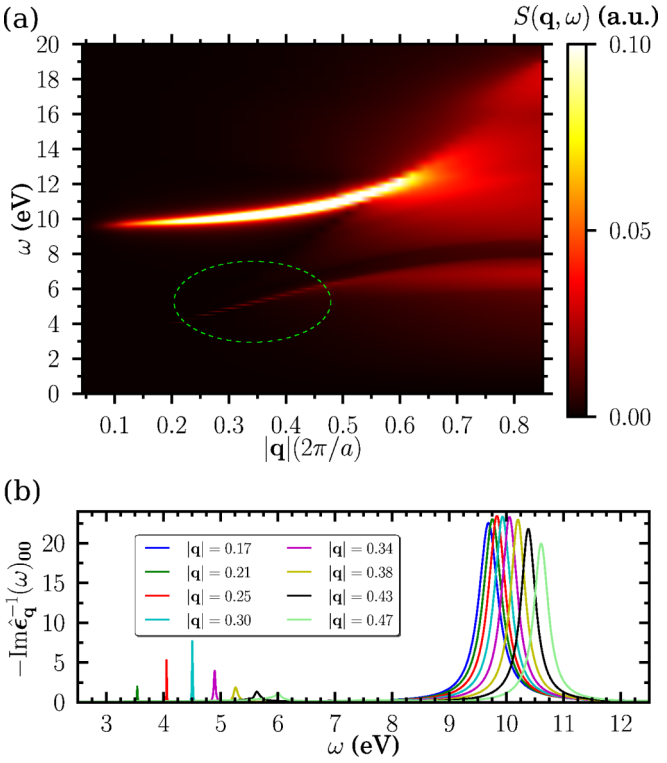

FIG. 3. (Color online) (a) and (b) Dynamical structure factor and energy-loss function of fcc Na at 75 GPa along the ΓL direction, respectively. In (a), the dashed (green) circle encloses the area where the anisotropic interband plasmon emerges. In (b), the values of the momentum considered are depicted in the inset (units of $2\pi/a$).

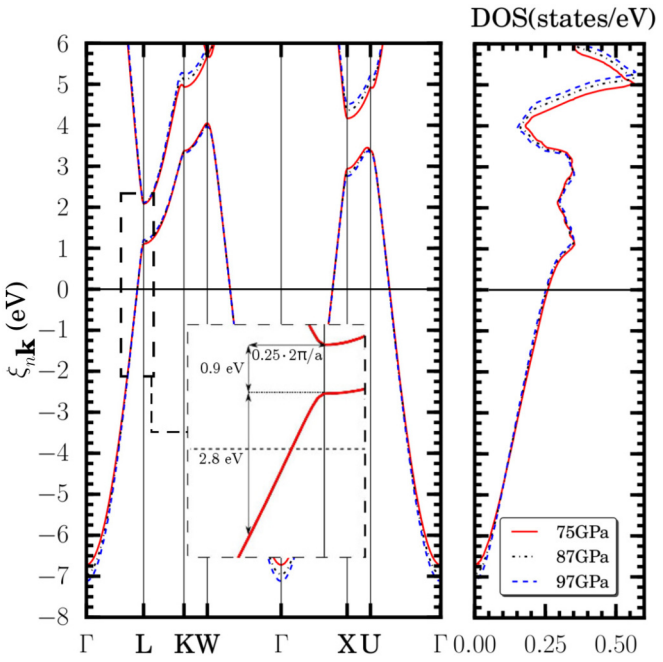

FIG. 4. (Color online) (Left panel) Electronic band structure of fcc Na at 75, 87, and 97 GPa. The inset shows the details of the band gap around high symmetry point L at 75 GPa. The Fermi level is indicated by the horizontal solid (black) line. (Right panel) Total DOS (states/eV).

2. *The fcc phase (65–105 GPa)*

At 65 GPa sodium undergoes a phase transformation from the bcc to the fcc structure. Unlike the rest of alkali metals, the Fermi surface of Na remains spherical up to ∼105 GPa [34]. From this point of view, the ground state of fcc Na retains the properties of simple metals. However, our calculations characterize an anisotropic plasmon along the ΓL direction directly associated with interband excitations, indicating a significant departure of the excited state properties of fcc Na from the simple metal behavior.

In Fig. 3(a) we display the calculated dynamical structure factor of fcc Na at 75 GPa along ΓL, showing a plasmon with parabolic dispersion that emerges at around 9.5 eV, in reasonable agreement with IXS data of Ref. [33], $\omega_p \simeq$ 9.25 eV. The evolution of the plasmon with respect to the momentum in the fcc phase has been included in Fig. 2 for 75, 87, and 97 GPa. Apart from showing a remarkable agreement with IXS data of Ref. [33], our calculations confirm that the plasmon dispersion is almost parabolic all over the stability pressure range of fcc Na.

It is noteworthy that the calculated dynamical structure factor depicted in Fig. 3(a) reveals a weaker second plasmon branch which does not follow at all the free-electron-like parabolic dispersion (see inside the dashed circle). The analysis of the energy-loss function [Fig. 3(b)] shows that this second branch emerges and disappears at finite values of the momentum, $|\mathbf{q}| \sim 0.2 \cdot 2\pi/a$ and $|\mathbf{q}| \sim 0.5 \cdot 2\pi/a$, respectively. Furthermore, the vanishingly small plasmon linewidth of Fig. 3(b) indicates that the associated collective excitation is practically undamped.

In order to identify the nature of this plasmon, we have performed an analysis of the energy-loss function along different directions, and we have not found any similar peak of $-\mathrm{Im}\,\hat{\epsilon}^{-1}_{\mathbf{q}}(\omega)_{\mathbf{00}}$ in any other direction. This fact reveals a strong anisotropy of the system that follows from the electronic band structure of fcc Na depicted in Fig. 4, which also displays important anisotropic features. Specifically, the free-electron-like band presents a gap at significantly different energies for different directions; the gap opens at ∼1 eV along ΓL, while for the rest of directions it opens around 3 to 4 eV. As shown in the next paragraph, the band structure has a direct impact on the electron-hole excitations and is the origin of the anisotropic plasmon we have found.

In Fig. 5 we display the real and imaginary parts of the dielectric function along ΓL and ΓX for various values of the momentum. Whereas for a given direction the calculations for different $\mathbf{q}$ share similar features, the results along ΓL and ΓX exhibit important differences. We first analyze the results along ΓL [Fig. 5(a)]. Focusing on $|\mathbf{q}| = 0.25 \cdot 2\pi/a$, we observe a decrease of $\mathrm{Im}\,\hat{\epsilon}_{\mathbf{q}}(\omega)_{\mathbf{00}}$ until it completely vanishes at ∼3.0 eV. This value coincides approximately with the energy at which intraband excitations along ΓL vanish due to the opening of a band gap (see inset of Fig. 4). The absence of electron-hole excitations remains up to ∼3.6 eV, where interband transitions begin; again, this energy coincides with the end of the band gap along ΓL. The strength of interband excitations is evidenced by the prominence of the peak at ∼3.7 eV in $\mathrm{Im}\,\hat{\epsilon}_{\mathbf{q}}(\omega)_{\mathbf{00}}$. Due to Kramers-Kronig relations [35], the peak in the imaginary

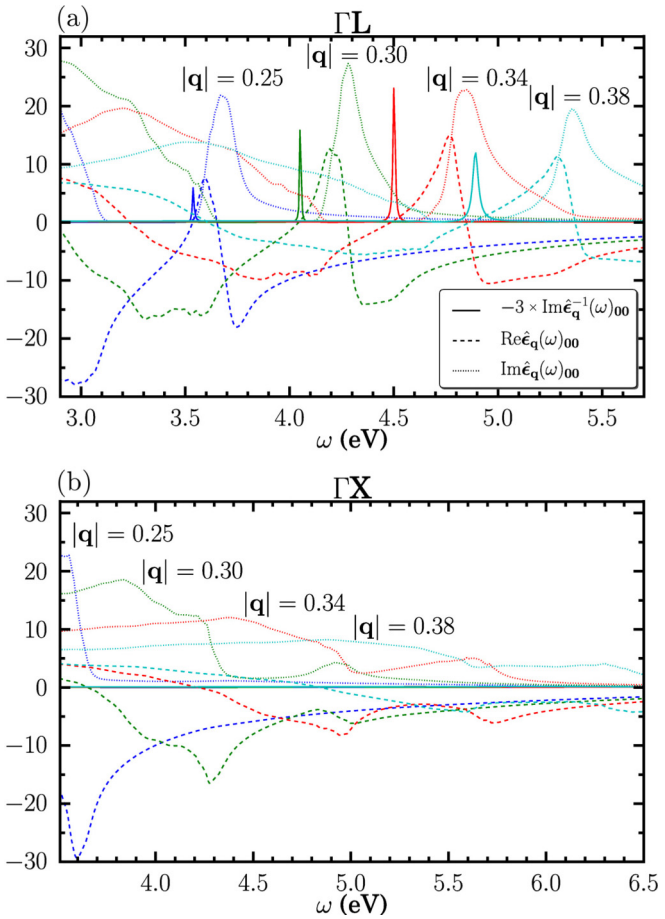

FIG. 5. (Color online) Real (dashed lines), imaginary (dotted lines), and inverse imaginary part (solid lines) of the dielectric function of fcc Na at 75 GPa along (a) ΓL and (b) ΓX. Note the different scale for $-\operatorname{Im}\hat{\boldsymbol{\epsilon}}_{\mathbf{q}}^{-1}(\omega)_{\mathbf{00}}$. Shown results are for $|\mathbf{q}| = 0.25$, 0.30, 0.34, and 0.38 (units of $2\pi/a$).

part drives the real part to the positive side, passing through zero at ∼3.6 eV and giving rise to the interband plasmon at that energy.

The above described situation remains very similar for $|\mathbf{q}| = 0.30$, 0.34, and $0.38 \cdot 2\pi/a$, the only relevant difference being an overall shift of all the features to higher energies, including the plasmon peak [see Fig. 5(a)]. For even higher momenta (results not shown) we find that the intraband and interband excitations overlap so that $\operatorname{Im}\hat{\boldsymbol{\epsilon}}_{\mathbf{q}}(\omega)_{\mathbf{00}}$ does not completely vanish in the intermediate energy region, leading to a significant broadening and weakening of the plasmon peak. At low momenta ($|\mathbf{q}| < 0.2 \cdot 2\pi/a$) the interband transitions are not sufficiently strong for driving $\operatorname{Re}\hat{\boldsymbol{\epsilon}}_{\mathbf{q}}(\omega)_{\mathbf{00}}$ to the positive part and, therefore, we do not find any plasmon peak in the energy-loss function.

The calculated results along ΓX, illustrated in Fig. 5(b), display two major differences with respect to the ones in Fig. 5(a). First, the intraband excitations end at significantly higher energies than in Fig. 5(a) due to the absence of band gaps in the band structure up to ∼3 eV from the Fermi energy (see Fig. 4). As a consequence, the intraband and interband excitations overlap even for $|\mathbf{q}| = 0.25 \cdot 2\pi/a$, preventing $\operatorname{Im}\hat{\boldsymbol{\epsilon}}_{\mathbf{q}}(\omega)_{\mathbf{00}}$ from vanishing. The second major difference

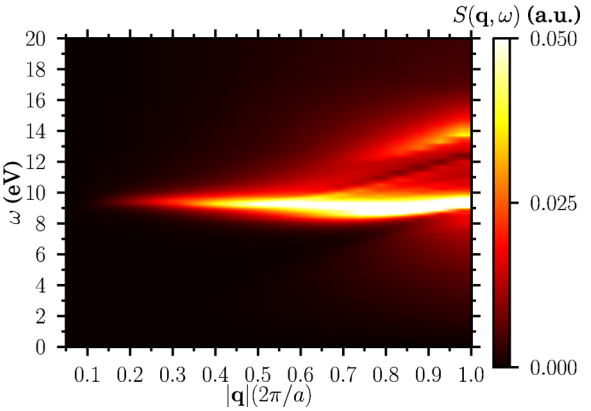

FIG. 6. (Color online) Dynamical structure factor of cI16 Na along ΓP at 105 GPa.

resides in the strength of the interband excitations, which is much weaker along the ΓX direction and is reflected by the relative decrease of the interband peak of $\operatorname{Im}\hat{\boldsymbol{\epsilon}}_{\mathbf{q}}(\omega)_{\mathbf{00}}$ as compared to that along ΓL. As a consequence, Kramers-Kronig relations do not drive $\operatorname{Re}\hat{\boldsymbol{\epsilon}}_{\mathbf{q}}(\omega)_{\mathbf{00}}$ to the positive part in the 3–7 eV energy range. Thus, unlike along ΓL, we do not find any interband plasmon along this or any other highly symmetric direction.

We have performed the same analysis at 87 and 97 GPa, verifying that the anisotropic plasmon along ΓL persists at these pressures as well. This is consistent with the associated band structures (see Fig. 4), which share very similar features as pressure increases in the fcc structure, including the band gap along ΓL at ∼1 eV above the Fermi level. Therefore, our calculations suggests that besides the free-electron-like plasmon at ∼10 eV, fcc Na presents an additional interband plasmon at ∼3.5–5.5 eV along ΓL all over its stability pressure range.

B. Complex phases of sodium

As characterized by several high pressure experiments [2,3,6], above 105 GPa sodium adopts considerably more complex structures than the previous bcc and fcc phases. Additionally, it exhibits clear fingerprints of pressure-induced complexity in this regime. As an example, the reflectivity of Na has been measured to drastically drop at low frequencies [4], indicating a clear departure from the expected free-electron-like behavior.

The connection between the reflectivity and the dielectric function of a material is given by

$$R(\omega) = \frac{[1 - n(\omega)]^2 + \kappa^2(\omega)}{[1 + n(\omega)]^2 + \kappa^2(\omega)}, \tag{19}$$

with $n(\omega) = \operatorname{Re}\sqrt{\hat{\boldsymbol{\epsilon}}_{\mathbf{q}}(\omega)_{\mathbf{00}}}$ and $\kappa(\omega) = \operatorname{Im}\sqrt{\hat{\boldsymbol{\epsilon}}_{\mathbf{q}}(\omega)_{\mathbf{00}}}$. In this section we will analyze the evolution of this quantity as a function of pressure.

1. The cI16 phase (105–118 GPa)

From 105 to 118 GPa, sodium adopts the cI16 structure. Interestingly, we have not found any anisotropic interband plasmon in this pressure range. This is exemplified in Fig. 6,

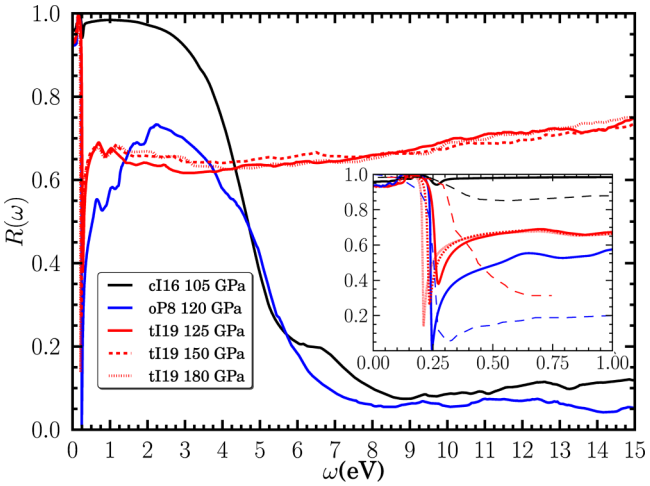

FIG. 7. (Color online) The calculated reflectivity spectrum of sodium in the phases cI16 (105 GPa), oP8 (120 GPa), and tI19 (125, 150, and 180 GPa). The inset addresses the 0–1.0 eV range, where we have also included synchrotron infrared spectroscopy data (long dashed lines) from Ref. [4].

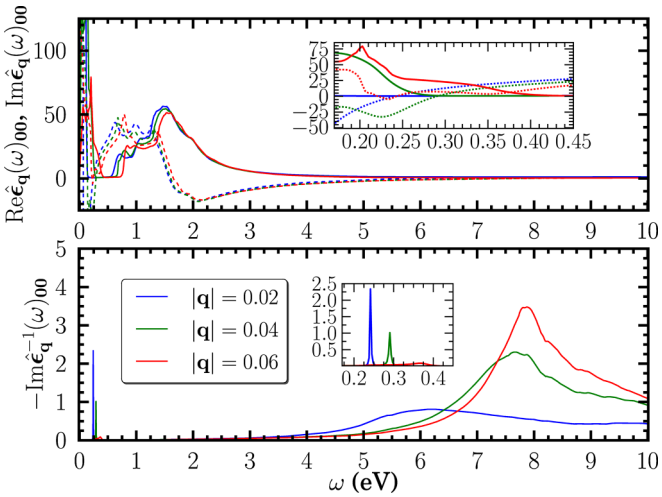

FIG. 8. (Color online) Dielectric function of oP8 Na at 120 GPa. Top panel: $\mathrm{Im}\,\hat{\boldsymbol{\epsilon}}_{\mathbf{q}}(\omega)_{\mathbf{00}}$ and $\mathrm{Re}\,\hat{\boldsymbol{\epsilon}}_{\mathbf{q}}(\omega)_{\mathbf{00}}$ are depicted by solid and dashed lines, respectively. Bottom panel: $-\mathrm{Im}\,\hat{\boldsymbol{\epsilon}}^{-1}_{\mathbf{q}}(\omega)_{\mathbf{00}}$. In both panels, results are shown for $|\mathbf{q}| = 0.02$, 0.04, and $0.06 \cdot 2\pi/a$. Both insets illustrate the ∼0.2–0.45 eV range.

where the calculated dynamical structure factor along the ΓP direction shows a single intraband plasmon at around 9.7 eV, which is ∼15% lower than the one predicted by the free-electron model. Furthermore, our calculations indicate that the evolution of the plasmon dispersion with respect to the momentum is not parabolic; in fact, Fig. 6 shows it is almost momentum independent along ΓP.

In Fig. 7 we show the calculated reflectivity [Eq. (19)] for cI16 Na. Our results indicate an almost complete light reflection from 0 to 3 eV. This property is in reasonable agreement with recent experiments [4] measuring a constant reflectivity $R(\omega) \simeq 0.85$ over the same frequency range. At 3 eV, the reflectivity starts a smooth decrease that ends at around 10 eV, where $R(\omega)$ is practically suppressed as a consequence of the intraband plasmon.

2. *The oP8 phase (118–125 GPa)*

Beyond 118 GPa, after a phase transformation favoring the oP8 structure [2], sodium exhibits an anomalous behavior associated with its optical response. This fact is clearly exemplified by Fig. 7, where the calculated reflectivity [Eq. (19)] in the oP8 phase shows a sudden dip at around 0.25 eV, vanishing almost completely. This behavior is in remarkable quantitative agreement with recent optical measurements showing a drop of the reflectivity to 0.05 at practically the same energy [4] (see inset of Fig. 7). After the dip, the reflectivity of oP8 Na partially recovers, but around 2 eV it starts a smooth decrease until ∼7 eV, where it becomes almost zero.

In Fig. 8 we analyze the dielectric function of oP8 Na. This figure reveals that the anomalous behavior of $R(\omega)$ in the optical range originates from a low-energy plasmon emerging at around 0.25 eV. This value is an order of magnitude smaller than the theoretically calculated plasma frequency reported in Ref. [4].

The low-energy plasmon characterized by our calculations shares common features with the one theoretically predicted in calcium under pressure [12], which also induces a dip in the calculated reflectivity. It is essentially undamped since both $\mathrm{Im}\,\hat{\boldsymbol{\epsilon}}_{\mathbf{q}}(\omega)_{\mathbf{00}}$ and $\mathrm{Re}\,\hat{\boldsymbol{\epsilon}}_{\mathbf{q}}(\omega)_{\mathbf{00}}$ become almost zero at $\omega \simeq 0.25$ eV, making the plasmon linewidth vanishingly small at this energy. For increasing values of the momentum, the linewidth of the low-energy plasmon starts broadening until $|\mathbf{q}| = 0.06 \cdot 2\pi/a$, where the peak in the energy-loss function is practically suppressed. At higher energies, our calculations evidence the existence of an intraband plasmon at around 6–8 eV that coincides with the final loss of reflectivity depicted in Fig. 7.

As shown in the top panel of Fig. 8, for $|\mathbf{q}| < 0.04 \cdot 2\pi/a$ our calculations evidence a gap between the intraband and interband excitations in the ∼0–0.6 eV energy range, where $\mathrm{Im}\,\hat{\boldsymbol{\chi}}^{\mathrm{KS}}_{\mathbf{q}}(\omega)_{\mathbf{00}}$ completely vanishes. Driven by the Kramers-Kronig relations, the gap and the subsequent interband excitations contributing to the imaginary part ($\omega > 0.6$ eV) force the real part of the dielectric function to become positive at $\omega \simeq 0.25$ eV, giving rise to the low-energy interband plasmon at that energy.

The relevant interband excitations contributing to $\mathrm{Im}\,\hat{\boldsymbol{\epsilon}}_{\mathbf{q}}(\omega)_{\mathbf{00}}$ in the $\mathbf{q}\to 0$ limit are characterized in the band structure of oP8 Na depicted in Fig. 9, alongside with the calculated DOS, which reproduces the weakening of the metallic character at the Fermi level reported in other works [4,5]. As indicated by the red arrows in Fig. 9, there exist quasiparallel occupied-unoccupied bands separated by 1–2 eV along various directions in reciprocal space: ZT, ΓZ, XS, and ΓY, among others. This feature is in agreement with previous theoretical band structure calculations [4,5]. The energy difference between these bands coincides with the interband excitations contributing to $\mathrm{Im}\,\hat{\boldsymbol{\epsilon}}_{\mathbf{q}}(\omega)_{\mathbf{00}}$ for $\omega \sim$ 1–2 eV (see top panel of Fig. 8), and are therefore directly responsible for the emergence of the low-energy plasmon at that energy.

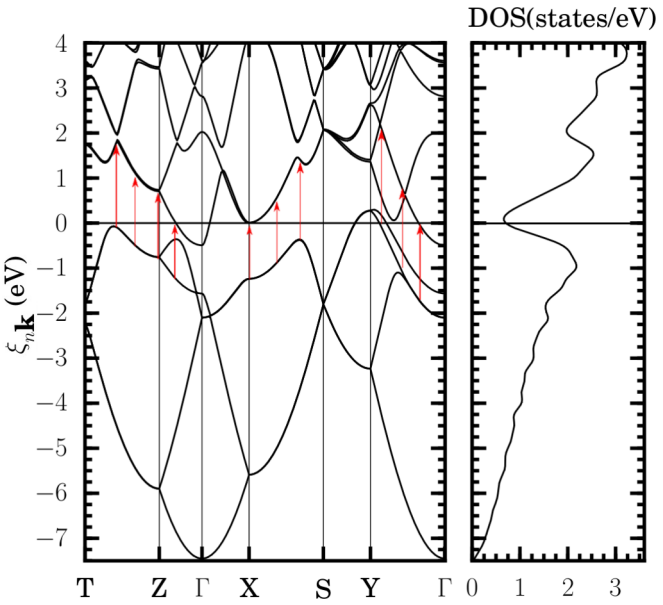

FIG. 9. (Color online) (Left panel) Electronic band structure of oP8 Na at 120 GPa. Red arrows depict the interband transitions responsible for the emergence of the low-energy plasmon. The Fermi level is indicated by the horizontal solid (black) line. (Right panel) Total DOS (states/eV).

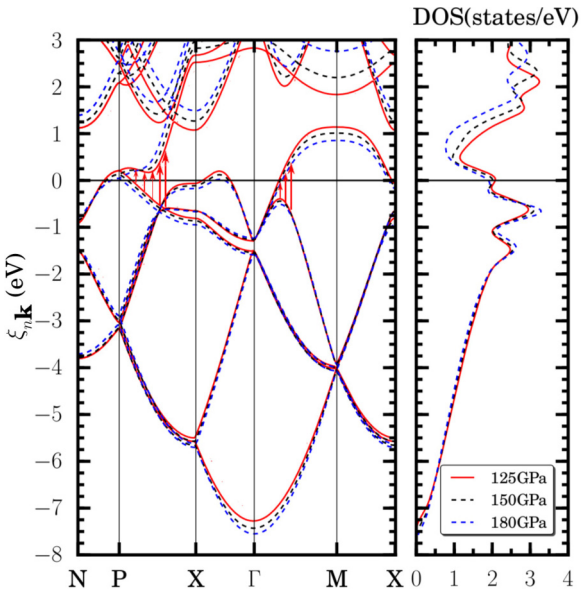

FIG. 11. (Color online) (Left panel) Electronic band structure of tI19 Na at 125, 150, and 180 GPa. Red arrows depict the interband transitions responsible for the emergence of the low-energy plasmon. The Fermi level is indicated by the horizontal solid (black) line. (Right panel) Total DOS (states/eV).

3. The tI19 phase (125–180 GPa)

At 125 GPa sodium adopts the tI19 structure [2]. As in the oP8 phase, we have also characterized a very low-energy plasmon, shown in Fig. 10, that induces a sudden dip on the optical reflectivity at around 0.25 eV (see Fig. 7), in qualitative agreement with optical measurements [4]. We find two major differences between the reflectivity spectrum of the oP8 and tI19 phases. First, the minimum of $R(\omega)$ ranges from ∼0.4 to ∼0.2 throughout the stability pressure range of the tI19 phase, whereas in the oP8 phase $R(\omega) \simeq 0$ at the dip. Second, unlike in the case of oP8 Na, the reflectivity of tI19 Na is almost totally recovered in the infrared regime, i.e., $R(\omega) \geqslant 0.6$ for $\omega > 0.75$ eV. These experimentally supported features [4] indicate that tI19 Na shows better metallic properties than oP8 Na, excluding a possible metal-insulator transition between the two phases.

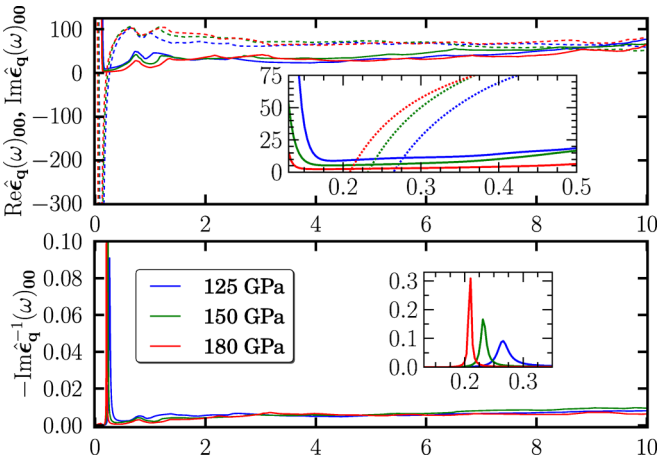

FIG. 10. (Color online) Dielectric function of tI19 Na at 125, 150, and 180 GPa for $|\mathbf{q}| = 0.03 \cdot 2\pi/a$ along ΓX. Top panel: $\mathrm{Im}\,\hat{\boldsymbol{\epsilon}}_{\mathbf{q}}(\omega)_{\mathbf{00}}$ and $\mathrm{Re}\,\hat{\boldsymbol{\epsilon}}_{\mathbf{q}}(\omega)_{\mathbf{00}}$ are depicted by solid and dashed lines, respectively. Bottom panel: $-\mathrm{Im}\,\hat{\boldsymbol{\epsilon}}^{-1}_{\mathbf{q}}(\omega)_{\mathbf{00}}$.

We have performed an analysis of the dielectric response function throughout the stability pressure range of tI19 Na from 125 to 180 GPa, as shown in Fig. 10. We find that the low-energy plasmon persists over all the studied domain. Moreover, our calculations indicate that the plasmon becomes undamped as pressure is increased, i.e., its linewidth decreases with increasing pressure [see Fig. 10(b)]. As shown in the inset of Fig. 10(a), $\mathrm{Im}\,\hat{\boldsymbol{\epsilon}}_{\mathbf{q}}(\omega)_{\mathbf{00}}$ does not completely vanish in the ∼0.2–0.5 eV range, where $\mathrm{Re}\,\hat{\boldsymbol{\epsilon}}_{\mathbf{q}}(\omega)_{\mathbf{00}}$ becomes vanishingly small. As a consequence, the resulting plasmon acquires a finite linewidth. Since $\mathrm{Im}\,\hat{\boldsymbol{\epsilon}}_{\mathbf{q}}(\omega)_{\mathbf{00}}$ decreases (approaches zero) with increasing pressure, so does the plasmon linewidth.

In Fig. 11 we show the calculated electronic band structure and DOS of tI19 Na at 125, 150, and 180 GPa. Our calculations are essentially in agreement with previously reported band structure calculations at 147 GPa [4]. The electronic excitations contributing to $\mathrm{Im}\,\hat{\boldsymbol{\epsilon}}_{\mathbf{q}}(\omega)_{\mathbf{00}}$ in the 0.5–1.0 eV range [see Fig. 10(a)] are characterized by red arrows, evidencing, as in the oP8 phase, the interband nature of the low-energy plasmon. Another important detail revealed by Fig. 11 is that tI19 Na develops two hole pockets, one around high symmetry point P and the other one halfway between Γ and X. Low-energy intraband excitations to these hole pockets are the reason why $\mathrm{Im}\,\hat{\boldsymbol{\epsilon}}_{\mathbf{q}}(\omega)_{\mathbf{00}}$ does not completely vanish in the ∼0.2–0.4 eV energy range. Furthermore, Fig. 11 indicates that the area of the hole pockets diminishes with increasing pressure, yielding weaker low-energy excitations at high pressures. We conclude that the damping of the low-energy plasmon revealed by

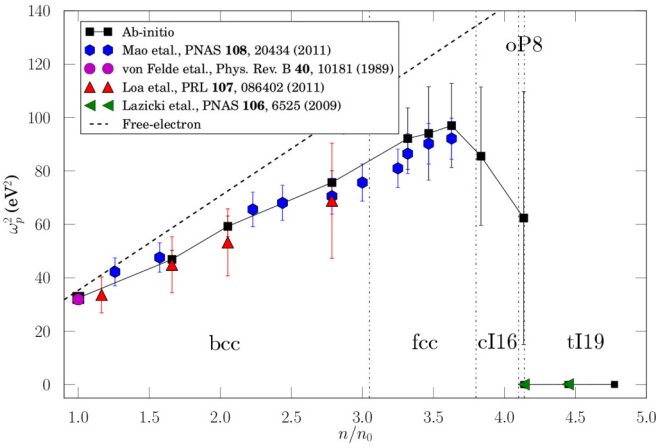

FIG. 12. (Color online) Plasmon dispersion of Na at $\mathbf{q}\rightarrow 0$ from 0 to 180 GPa with respect to the density. Squares (black) represent our *ab initio* calculations including the plasmon linewidth, and solid lines are simple guides to the eye. Experimental data are taken from Refs. [4,31–33]. Vertical dot-dashed lines separate different phases of Na. The dashed line denotes the free-electron dispersion $\omega_p^2 = 4\pi n/m^2$.

Fig. 10(b) is directly associated with the evolution of the hole pockets under pressure.

IV. CONCLUSIONS

To conclude our analysis, in Fig. 12 we illustrate the plasmon evolution of sodium in the optical limit ($\mathbf{q}\rightarrow 0$) as a function of the density, covering all the phases from 0 to 180 GPa. This figure makes it clear that sodium increasingly departs from the free-electron-like model as its density is raised. In particular, the figure evidences a complete breakdown of the free-electron-like picture at the high pressure phases cI16, oP8, and tI19. Classically, the plasmon energy should increase with the density, but our calculations show a marked decrease in the plasmon energy in the cI16 and oP8 phases, accompanied by a huge increase of the plasmon linewidth. Finally, our calculations predict the absence of intraband plasmons in the tI19 phase, where only the low-energy interband plasmon is present. Therefore, sodium represents a clear example of how pressure can induce great complexity even in the simplest elements.

In this paper we have presented theoretical *ab initio* calculations regarding the dielectric response of bulk sodium in its five known metallic phases from 0 to 180 GPa at room temperature. We have employed a formalism based on a Wannier interpolation scheme that provides a very accurate sampling of reciprocal space and allows the resolution of sharp features associated with the dielectric function. In this way we predict the existence of a low-energy plasmon in the high pressure phases oP8 and tI19 that explains the anomalous behavior in the recently measured optical reflectivity [4], also reproduced by our calculations. The combined analysis of the KS response function and the electronic band structure reveals the interband nature of this low-energy plasmon, associated with electron-hole transitions between a network of quasiparallel occupied-unoccupied bands. Additionally, our calculations characterize an anisotropic interband plasmon all along the stability pressure range of the fcc configuration (65 to 105 GPa), revealing an unexpected departure of fcc Na from the free-electron model. This remarkable plasmon is found exclusively along the ΓL direction due to an anisotropic non-free-electron-like band structure effect.

ACKNOWLEDGMENTS

We are very grateful to Ion Errea for many fruitful discussions. The authors acknowledge financial support from UPV/EHU (Grant No. IT-366-07) and the Spanish Ministry of Science and Innovation (Grant No. FIS2010-19609-C02-00). Computer facilities were provided by the Donostia International Physics Center (DIPC).

[1] J. B. Neaton and N. W. Ashcroft, Phys. Rev. Lett. **86**, 2830 (2001).
[2] E. Gregoryanz, L. F. Lundegaard, M. I. McMahon, C. Guillaume, R. J. Nelmes, and M. Mezouar, Science **320**, 1054 (2008).
[3] Y. Ma, M. Eremets, A. R. Oganov, Y. Xie, I. Trojan, S. Medvedev, A. O. Lyakhov, M. Valle, and V. Prakapenka, Nature (London) **458**, 182 (2009).
[4] A. Lazicki, A. F. Goncharov, V. V. Struzhkin, R. E. Cohen, Z. Liu, E. Gregoryanz, C. Guillaume, H. Mao, and R. J. Hemley, Proc. Natl. Acad. Sci. USA **106**, 6525 (2009).
[5] L. F. Lundegaard, E. Gregoryanz, M. I. McMahon, C. Guillaume, I. Loa, and R. J. Nelmes, Phys. Rev. B **79**, 064105 (2009).
[6] M. Hanfland, K. Syassen, L. Loa, N. E. Christensen, and D. L. Novikov, Poster at 2002 High Pressure Gordon Conference (2002).
[7] B. Rousseau, Y. Xie, Y. Ma, and A. Bergara, Eur. Phys. J. B **81**, 1 (2011).
[8] A. Rodriguez-Prieto and A. Bergara, Phys. Rev. B **72**, 125406 (2005).
[9] A. R. Oganov, Y Ma, Y. Xu, I. Errea, A. Bergara, and A. O. Lyakhov, Proc. Natl. Acad. Sci. USA **107**, 7646 (2010).
[10] J. B. Neaton and N. W. Ashcroft, Nature (London) **400**, 141 (1999).
[11] V. M. Silkin, A. Rodriguez-Prieto, A. Bergara, E. V. Chulkov, and P. M. Echenique, Phys. Rev. B **75**, 172102 (2007).
[12] I. Errea, B. Rousseau, A. Eiguren, and A. Bergara, Phys. Rev. B **86**, 085106 (2012).
[13] B. Rousseau, A. Eiguren, and A. Bergara, Phys. Rev. B **85**, 054305 (2012).
[14] E. Runge and E. K. U. Gross, Phys. Rev. Lett. **52**, 997 (1984).
[15] M. Petersilka, U. J. Gossmann, and E. K. U. Gross, Phys. Rev. Lett. **76**, 1212 (1996).
[16] J. P. Perdew and A. Zunger, Phys. Rev. B **23**, 5048 (1981).
[17] C. Bowen, G. Sugiyama, and B. J. Alder, Phys. Rev. B **50**, 14838 (1994).

[18] S. L. Adler, Phys. Rev. **126**, 413 (1962).
[19] N. Marzari and D. Vanderbilt, Phys. Rev. B **56**, 12847 (1997).
[20] W. M. Saslow and G. F. Reiter, Phys. Rev. B **7**, 2995 (1973).
[21] B. Farid, G. E. Engel, R. Daling, and W. van Haeringen, Phys. Rev. B **44**, 13349 (1991).
[22] K. Sturm, Adv. Phys. **31**, 1 (1982).
[23] P. Giannozzi *et al.*, J. Phys.: Condens. Matter **21**, 395502 (2009).
[24] H. J. Monkhorst and J. D. Pack, Phys. Rev. B **13**, 5188 (1976).
[25] http://opium.sourceforge.net/
[26] http://elk.sourceforge.net/
[27] A. Mostofi, J. Yates, Y. Lee, I. Souza, D. Vanderbilt, and I. Marzari, Comput. Phys. Commun. **178**, 685 (2008).
[28] M. Hanfland, I. Loa, and K. Syassen, Phys. Rev. B **65**, 184109 (2002).
[29] G. D. Mahan, *Many-Particle Physics* (Plenum, New York, 2000).
[30] X. Wang, J. R. Yates, I. Souza, and D. Vanderbilt, Phys. Rev. B **74**, 195118 (2006).
[31] A. vom Felde, J. Sprösser-Prou, and J. Fink, Phys. Rev. B **40**, 10181 (1989).
[32] I. Loa, K. Syassen, G. Monaco, G. Vanko, M. Krisch, and M. Hanfland, Phys. Rev. Lett. **107**, 086402 (2011).
[33] H.-K. Mao, Y. Ding, Y. Xiao, P. Chow, J. Shu, S. Lebgue, A. Lazicki, and R. Ahuja, Proc. Natl. Acad. Sci. USA **108**, 20434 (2011).
[34] Y. Xie, Y. M. Ma, T. Cui, Y. Li, J. Qiu, and G. T. Zou, New J. Phys. **10**, 063022 (2008).
[35] D. Pines and P. Nozieres, *The Theory of Quantum Liquids* (Benjamin, New York, 1966), Vol. 1.